# Spectral image fusion from compressive measurements

Edwin Vargas, Oscar Espitia, Henry Arguello, Jean-Yves Tourneret

## To cite this version:

Edwin Vargas, Oscar Espitia, Henry Arguello, Jean-Yves Tourneret. Spectral image fusion from compressive measurements. IEEE Transactions on Image Processing, 2019, 28 (5), pp.2271-2282. 10.1109/TIP.2018.2884081 . hal-02052028

**HAL Id: hal-02052028**

**https://hal.science/hal-02052028v1**

Submitted on 28 Feb 2019

This is an author's version published in: http://oatao.univ-toulouse.fr/21908

**Official URL:**

https://doi.org/10.1109/TIP.2018.2884081

**To cite this version:**

Vargas, Edwin and Espitia, Oscar and Arguello, Henry and Tourneret, Jean-Yves Spectral image fusion from compressive measurements. (2019) IEEE Transactions on Image Processing, 28 (5). 2271-2282. ISSN 1057-7149

# Spectral Image Fusion From Compressive Measurements

Edwin Vargas, Óscar Espitia, Henry Arguello and Jean-Yves Tourneret

*Abstract*—**Compressive spectral imagers reduce the number of sampled pixels by coding and combining the spectral information. However, sampling compressed information with simultaneous high spatial and high spectral resolution demands expensive high-resolution sensors. This paper introduces a model allowing data from high spatial/low spectral and low spatial/high spectral resolution compressive sensors to be fused. Based on this model, the compressive fusion process is formulated as an inverse problem that minimizes an objective function defined as the sum of a quadratic data fidelity term and smoothness and sparsity regularization penalties. The parameters of the different sensors are optimized and the choice of an appropriate regularization is studied in order to improve the quality of the high resolution reconstructed images. Simulation results conducted on synthetic and real data, with different compressive sampling imagers, allow the quality of the proposed fusion method to be appreciated.**

*Index Terms*—**Spectral imaging, compressive sampling, data fusion, remote sensing.**

## I. INTRODUCTION

HYPERSPECTRAL imaging allows the identification and visualization of materials in a scene via spectroscopic analysis. It is important in many applications such as Earth observation [1]–[3], geology [4], food safety [1], [2] and medical imaging [5]. The extraction of useful information from hyperspectral (HS) images involves advanced inference methods trying to overcome the problems related to the high dimensionality of these images and to their low spatial or spectral resolutions. These methods often require solving inverse problems that are considered in many research topics, including compressive acquisition, super-resolution, and fusion (see [1] for descriptions).

Remote sensing imagers usually deliver images with either high spatial/low spectral or high spectral/low spatial resolutions. However, applications involving detection, tracking, and classification require images with both high spectral and high spatial resolutions. These requirements are at the origin of many works related to the fusion of images with different spatial and spectral resolutions [6]. On the other hand, most imaging systems deliver data with a significant redundancy, which can be reduced by using compressive sampling (CS) [7], [8]. CS is based on the fact that many natural signals can be represented with a few coefficients in some basis and can thus be efficiently compressed. It has been shown that the use of appropriate sensing matrices allows the performance of signal reconstruction methods to be close to the one obtained without using CS [9]. However, designing systems characterized by low-cost compressed measurements with high spatial and high spectral resolutions is still a challenging problem.

There are several approaches for compressing spectral data. This paper focusses on two classes of imagers that have been implemented in practical applications, which capture a spectral scene using a single or multiple 2D snapshots obtained with different sampling patterns: $i$) spatial coding-based CS imagers, such as the coded aperture snapshot spectral imager (CASSI) [10] and $ii$) spectral coding-based spectral imagers, such as the spatio-spectral encoded compressive spectral imager (SSCSI) [11], or the colored-CASSI [8]. At this point, it is interesting to mention that other theoretical approaches have been studied for compressive spectral imaging, such as the hyperspectral coded aperture (HYCA) [12] or the compressive-projection principal component analysis [13]. However, these approaches have, to the author knowledge, never been applied in practical applications.

This paper introduces a model allowing high spatial and spectral resolution images to be reconstructed from two images acquired with compressive spectral imagers. The observed images are assumed to result from spectral and/or spatial degradations of a high resolution (HR) image (to be recovered) acquired with a CS operation. The HR image of interest is stacked into a column vector $\mathbf{f} = [f_1, ..., f_{N^2L}]^T \in \mathbb{R}^{N^2L}$, where $N^2$ is the number of image pixels and $L$ is the number of spectral bands. We also assume that $\mathbf{f}$ can be decomposed as $\mathbf{f} = \mathbf{\Psi}\mathbf{x}$, where $\mathbf{x} \in \mathbb{R}^{N^2L}$ contains only $N_z \ll N^2L$ nonzero elements and $\mathbf{\Psi} \in \mathbb{R}^{N^2L \times N^2L}$ is an operator expressing the fact that the image is sparse in a given domain. This decomposition assumes that the image of interest can be described as a linear combination of a few atoms belonging to the dictionary $\mathbf{\Psi}$.

---

This work was supported in part by the Department of Science, Technology and Innovation, COLCIENCIAS, in part by the Ministerio de Educación Nacional of Colombia, in part by ICETEX, and in part by the French Government under grant ECOS Nord, Intercambio de Investigadores Colombia-Francia, with the Project "Diseño de Aperturas Codificadas de Color Para Realizar Separación Espectral de Imágenes de Productos agrícolas Adquiridas Mediante Muestreo Compresivo." Part of this work was also conducted within the STIC-AmSud project HYPERMED. The associate editor coordinating the review of this manuscript and approving it for publication was Dr. Chandra Sekhar Seelamantula. *(Corresponding author: Jean-Yves Tourneret.)*

E. Vargas is with the Department of Electrical Engineering, Universidad Industrial de Santander, 680002 Bucaramanga, Colombia.

Ó. Espitia and H. Arguello are with the Department of Systems Engineering and Informatics, Universidad Industrial de Santander, 680002 Bucaramanga, Colombia.

J.-Y. Tourneret is with the University of Toulouse, INP-ENSEEIHT/IRIT/TéSA, 31071 Toulouse, France (e-mail: jean-yves.tourneret@enseeiht.fr).

Digital Object Identifier 10.1109/TIP.2018.2884081

The noiseless observations considered in this work are HS and multispectral (MS) compressed images denoted as $\mathbf{y}_{\mathrm{h}} = \mathbf{\Phi}_{\mathrm{h}}\mathbf{f}$ and $\mathbf{y}_{\mathrm{m}} = \mathbf{\Phi}_{\mathrm{m}}\mathbf{f}$. Note that the variables with subindex $_{\mathrm{h}}$ and subindex $_{\mathrm{m}}$ used in this paper will refer to variables associated with HS and MS images, respectively. The matrices $\mathbf{\Phi}_{\mathrm{h}}$ and $\mathbf{\Phi}_{\mathrm{m}}$ are defined in the general case of $K_{\mathrm{h}}$ and $K_{\mathrm{m}}$ snapshots as $\mathbf{\Phi}_{\mathrm{h}} = [(\mathbf{\Phi}_{\mathrm{h}}^{1})^T, \cdots, (\mathbf{\Phi}_{\mathrm{h}}^{K_{\mathrm{h}}})^T]^T$ and $\mathbf{\Phi}_{\mathrm{m}} = [(\mathbf{\Phi}_{\mathrm{m}}^{1})^T, \cdots, (\mathbf{\Phi}_{\mathrm{m}}^{K_{\mathrm{m}}})^T]^T$, where $\mathbf{\Phi}_{\mathrm{h}}^{k_{\mathrm{h}}} = \mathbf{\Phi}^{k_{\mathrm{h}}}(N_{\mathrm{h}}, L)\mathbf{B}$, $\mathbf{\Phi}_{\mathrm{m}}^{k_{\mathrm{m}}} = \mathbf{\Phi}^{k_{\mathrm{m}}}(N, L_{\mathrm{m}})\mathbf{L}$ and where $\mathbf{\Phi}^{k_{\mathrm{h}}}(N_{\mathrm{h}}, L) \in \mathbb{R}^{V_{\mathrm{h}} \times N_{\mathrm{h}}^2 L}$ and $\mathbf{\Phi}^{k_{\mathrm{m}}}(N, L_{\mathrm{m}}) \in \mathbb{R}^{V_{\mathrm{m}} \times N^2 L_{\mathrm{m}}}$ are appropriate sensing matrices, with $V_{\mathrm{h}}, V_{\mathrm{m}} \ll N^2 L$, $k_{\mathrm{h}} = 1, \cdots, K_{\mathrm{h}}$ and $k_{\mathrm{m}} = 1, \cdots, K_{\mathrm{m}}$. The matrix $\mathbf{B} \in \mathbb{R}^{N_{\mathrm{h}}^2 L \times N^2 L}$ $(N_{\mathrm{h}} \ll N)$ is an operator associated with spatial blurring and downsampling, and $\mathbf{L} \in \mathbb{R}^{N^2 L_{\mathrm{m}} \times N^2 L}$ $(L_{\mathrm{m}} \ll L)$ is a filtering operator transforming the spectral content of the reference image into the spectral bands of the MS image. Note that $\mathbf{\Phi}_{\mathrm{h}}^{k_{\mathrm{h}}} \in \mathbb{R}^{V_{\mathrm{h}} \times N^2 L}$ and $\mathbf{\Phi}_{\mathrm{m}}^{k_{\mathrm{m}}} \in \mathbb{R}^{V_{\mathrm{m}} \times N^2 L}$ are HS and MS CS matrices that perform both compression and decimation operations simultaneously.

The problem addressed in this paper is the estimation of the HR image $\mathbf{f}$ (assumed to be sparse in the $\mathbf{\Psi}$ domain) from the noisy measurements $\tilde{\mathbf{y}}_{\mathrm{h}} = \mathbf{y}_{\mathrm{h}} + \mathbf{n}_{\mathrm{h}}$ and $\tilde{\mathbf{y}}_{\mathrm{m}} = \mathbf{y}_{\mathrm{m}} + \mathbf{n}_{\mathrm{m}}$, where $\mathbf{n}_{\mathrm{h}}$ and $\mathbf{n}_{\mathrm{m}}$ are the HS and MS noise vectors (after compression). Note that the observation model defined by $\tilde{\mathbf{y}}_{\mathrm{h}}$ and $\tilde{\mathbf{y}}_{\mathrm{m}}$ is similar to the one introduced in [14], except that the unknown image $\mathbf{f}$ has been vectorized and that the observed images have been compressed leading to a reduced cost for their acquisition. The main objective of this paper is to show that we can exploit sparsity to fuse compressed spectral images. Note that sparsity guarantees that the inverse problem consisting of estimating $\mathbf{f}$ from $\tilde{\mathbf{y}}_{\mathrm{h}}$ and $\tilde{\mathbf{y}}_{\mathrm{m}}$ is well-posed [15].

The problem of fusing multi-resolution images has received much attention in the literature [14], [16]–[19]. Some recent works have also been devoted to the fusion of compressive data in order to increase the interpretability of the images [20], [21]. We argue that the use of compressive measurements with appropriate sensing matrices can lead to high-quality image reconstruction and that compressive measurements have favorable properties to solve the multisensor fusion problem. We propose to formulate the fusion problem as an inverse problem that minimizes an appropriate objective function. This function is classically built as the sum of a quadratic data fidelity term and appropriate regularizations. The regularizations considered in this paper include a total variation (TV) term ensuring smoothness of the solution and a sparsity term ensuring that the solution is sparse in a given dictionary. To ensure a good performance of the proposed image reconstruction method, a specific attention will be devoted to the design of the sensing matrices in order to obtain good reconstruction performance.

The outline of this paper is as follows: Section 2 gives a detailed background on compressive spectral imagers. Section 3 recalls how HS and MS compressed data can be practically constructed using the principles of the CASSI system. Section 4 introduces the inverse problem investigated in this work for the fusion of HS and MS measurements. Experimental results are presented in Section 5, allowing the performance of the proposed fusion method to be appreciated. Concluding remarks are finally reported in Section 6.

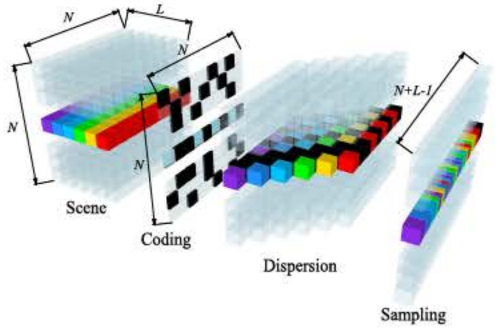

Fig. 1. Compression with spatial coding. The spectral scene is coded and dispersed by a dispersive element (grating or prism). Thus, the detector creates a 2D projection of the coded and shifted scene.

## II. COMPRESSIVE SPECTRAL IMAGERS

This section recalls the principles of two classes of imagers that have been implemented in practical applications, based on spatial and spectral coding, and other theoretical approaches that have been studied for compressive spectral imaging are also presented. The structure of the sensing matrices $\mathbf{\Phi}^k(N, L)$ will be introduced.

### *A. Spatial Coding Based Imager: CASSI*

CS imagers capture a spectral scene using 2D projections that are obtained with different sampling patterns. For instance, the coded aperture snapshot spectral imager (CASSI) system uses a coded aperture that replaces the entrance slit of a dispersive spectrometer by a much wider field stop, inside which is inserted a binary-coded mask. This mask attempts to create a transmission pattern. The encoded light, transmitted by the coded mask within the field stop is then passed through a standard spectrometer back-end (i.e., collimating lens, disperser, reimaging lens, and detector array). This compression procedure is illustrated in Fig. 1.

The CASSI projections can be discretized as

$$\mathbf{y}^k = \mathbf{\Phi}^k(N, L)\mathbf{f} \tag{1}$$

where $k = 1, ..., K$ corresponds to the $k$th single snapshot of a scene, $\mathbf{y}^k \in \mathbb{R}^{N(N+L-1)}$ contains the measurement stacked into a column vector, $\mathbf{f} \in \mathbb{R}^{N^2\ L}$ contains the values of the discrete source spectral density, and $\mathbf{\Phi}^k(N, L) \in \mathbb{R}^{N(N+L-1) \times N^2 L}$ is the sparse modulation matrix of the $s$th CASSI snapshot (that performs both coding and shifting operations, as mentioned before). The matrix $\mathbf{\Phi}^k(N, L)$ has ideally binary entries, as illustrated in Fig. 2. Note that its structure consists of a set of diagonal patterns, that repeat along the horizontal direction, such that one spatial dimension is shifted downward, as many times as the number of spectral bands. Each diagonal element is due to a transmission pattern $\mathbf{T}^k \in \mathbb{R}^{N \times N}$, that has been vectorized column-wise. Note that other patterns of diagonal elements are vertically stacked when several snapshots are considered by the system.

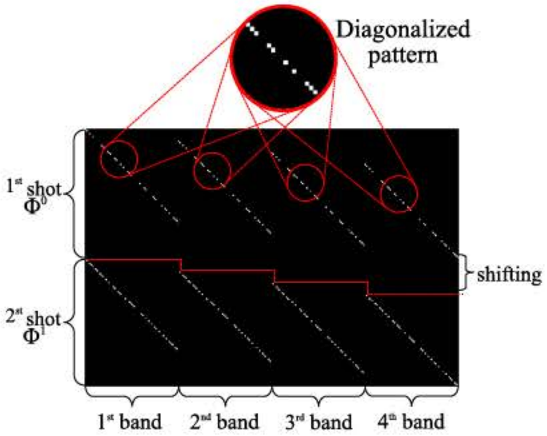

Fig. 2. CASSI coded projection operator (for capturing 4 spectral bands by using 2 different sampling patterns and $K = 2$ snapshots).

The matrix $\mathbf{\Phi}^k(N, L)$ used in the CASSI system can be constructed from the following $n \times n$ permutation matrix

$$\mathbf{\Lambda}_n = \begin{bmatrix} 0 & \cdots & 0 & 1 \\ 1 & & 0 & 0 \\ 0 & \ddots & 0 & 0 \\ 0 & 0 & 1 & 0 \end{bmatrix}. \tag{2}$$

More precisely, if we discretize the transmission pattern as the column vector $\mathbf{t} \in \mathbb{R}^{N^2}$, the matrix $\mathbf{\Phi}^k(N, L)$ can be expressed as

$$\mathbf{\Phi}^k(N, L) = \sum_{i=0}^{L-1} (\mathbf{\Lambda}_V)^{iN} [\mathrm{diag}(\mathbf{t}^k), \mathbf{0}]^T \mathbf{I}_{\mathrm{C}} (\mathbf{\Lambda}_{N^2 L})^{-iN^2} \tag{3}$$

where $V = N(N + L - 1)$, $\mathrm{diag}(\boldsymbol{\chi})$ is a diagonal matrix formed from the vector $\boldsymbol{\chi}$, $\mathbf{0}$ is the $N^2 \times N(L-1)$ zero matrix, $\mathbf{I}_{\mathrm{C}} = [\mathbf{I}, \mathbf{0}_{\mathrm{C}}]$, $\mathbf{I} \in \mathbb{R}^{N^2 \times N^2}$ is the $N^2 \times N^2$ identity matrix, and $\mathbf{0}_{\mathrm{C}}$ is the $N^2 \times N^2(L-1)$ zero matrix.

### *B. Spatio-Spectral Coding Based Imager: SSCSI*

Another state-of-the-art compressive imager is the spatio spectral encoded compressive spectral imager (SSCSI). Here, the coded sensor image is achieved by applying a diffraction grating to disperse the light into the spectrum plane and inserting a coded attenuation mask between the spectrum plane and the sensor plane. The diffraction grating on the image plane maps the spectral dimension of the light to its angular dimension. A ray incident on the diffraction grating produces multiple diffracted outgoing rays in different directions with different spectral bands, as illustrated in Fig. 3. The compression procedure of the SSCSI can also be discretized as in (1), i.e., as $\mathbf{y}^k = \mathbf{\Phi}^k(N, L)\mathbf{f}$, where $\mathbf{y}^k \in \mathbb{R}^{N^2}$ is the $k$th vectorized sensor image, and $\mathbf{\Phi}^k(N, L) \in \mathbb{R}^{N^2 \times N^2 L}$ is the $k$th modulation matrix. The $L$ vectorized spectral bands, stacked in a column vector, are modulated by each modulation matrix $\mathbf{\Phi}^k(N, L) \in \mathbb{R}^{N^2 \times N^2 L}$, which contains the sheared pattern from the mask $\mathbf{T}^k \in \mathbb{R}^{N \times (N+L-1)}$ on its diagonal. The resulting sparse modulation matrix with binary entries is displayed in Fig. 4. Note that it is also structured as a set of diagonal patterns. However, the patterns do not repeat horizontally, allowing spectral coding. If we discretize the transmission pattern as the column vector $\mathbf{t}^k \in \mathbb{R}^V$, the $\mathbf{\Phi}^k(N, L)$ matrix for the SSCSI is defined as

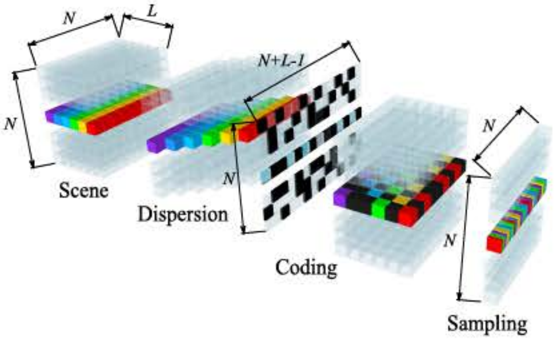

Fig. 3. Compression with spectral coding.

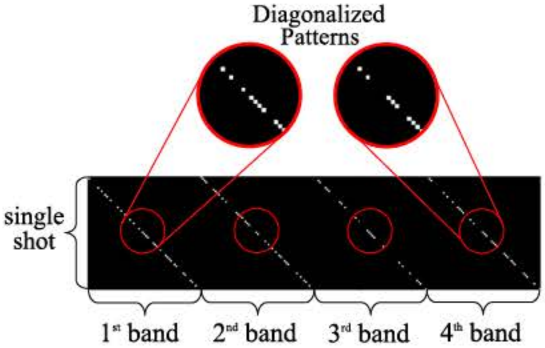

Fig. 4. SSCSI coded projection operator (for capturing 4 spectral bands by spectral coding and a single snapshot, i.e., $L = 4$ and $K = 1$).

$$\begin{aligned} &\mathbf{\Phi}^k(N, L) \\ &\quad = \sum_{i=0}^{L-1} \mathbf{I}_{\mathrm{S}} (\mathbf{\Lambda}_V)^{iN} [\mathrm{diag}(\mathbf{t}^k)] (\mathbf{\Lambda}_V)^{-iN} \mathbf{I}_{\mathrm{S}}^T \mathbf{I}_{\mathrm{C}} (\mathbf{\Lambda}_{N^2 L})^{-iN^2} \end{aligned} \tag{4}$$

where $\mathbf{I}_{\mathrm{S}} = [\mathbf{I}, \mathbf{0}]$.

### *C. Gaussian Measurement Matrices*

Some CS systems compute a few random projections of the observations using, e.g., Gaussian independent and identically distributed (i.i.d.) vectors allowing spatial/spectral coding [12], [13], [22]. These systems have proved their efficiency for data reconstruction and will be used as a benchmark compared with the proposed methods. These systems can be also described by the matrix-vector form (1). However, the coded projection operator is expressed as a sparse modulation matrix with Gaussian entries, as illustrated in Fig. 5. Note that the measurement matrix in Fig. 5 is built using diagonal Gaussian vectors. After discretizing the Gaussian patterns into a column vector $\mathbf{t}_i^k \in \mathbb{R}^{N^2}$ $(i = 0, \cdots, L-1)$, the matrix $\mathbf{\Phi}^k(N, L)$ is constructed as

$$\mathbf{\Phi}^k(N, L) = \sum_{i=0}^{L-1} [\mathrm{diag}(\mathbf{t}_i^k)] \mathbf{I}_{\mathrm{C}} (\mathbf{\Lambda}_{N^2 L})^{-iN^2}. \tag{5}$$

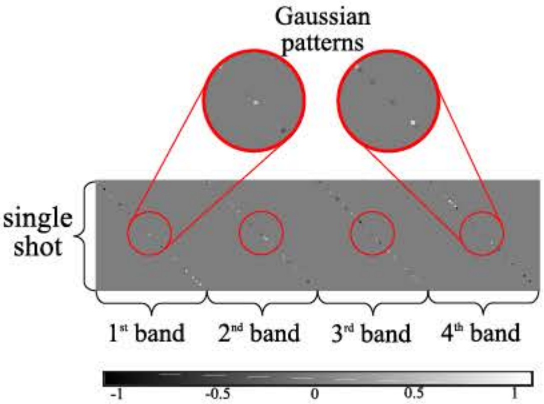

Fig. 5. Gaussian coded projection operator (for capturing 4 spectral bands by using i.i.d. vectors as sampling patterns and a single snapshot, i.e., $L = 4$ and $K = 1$).

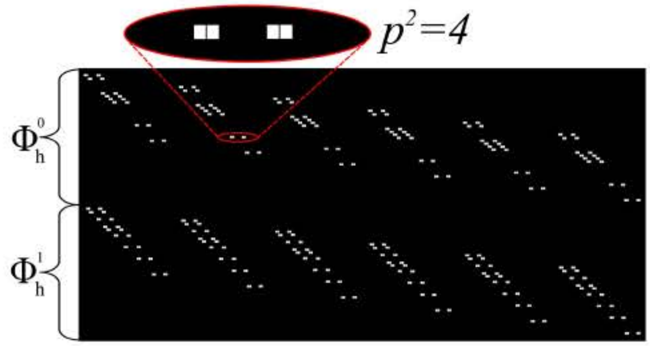

Fig. 6. HS CASSI measurement matrix $\mathbf{\Phi}_\mathrm{h}$ for $L = 6$, $K_\mathrm{h} = 2$ and $p = 2$.

## III. MEASUREMENT MATRICES USED IN THE CASSI SYSTEM FOR THE CS IMAGE FUSION PROBLEM

The structure of the measurement matrices $\mathbf{\Phi}_\mathrm{h}$ and $\mathbf{\Phi}_\mathrm{m}$ can have a strong impact on the quality of the reconstructed images. This section introduces the constraints associated with these matrices for the CASSI system and proposes a way to design these matrices for the fusion of HS and MS images. Note that these considerations have also to be taken into account for the SSCSI and Gaussian systems.

### *A. Structure of the Sensing Matrices $\mathbf{\Phi}_h$ and $\mathbf{\Phi}_m$*

Fig. 6 shows an instance of the structure of the HS sparse modulation matrix $\mathbf{\Phi}_\mathrm{h}$ for the CASSI system. Each row of this matrix performs a linear combinations of $p^2$ adjacent pixels, which means that the scene projected onto this matrix, besides being compressed, will be degraded spatially by a factor $p$ (e.g., $p = 2$ in Fig. 6). The matrix $\mathbf{\Phi}_\mathrm{h}^k$ associated with the $k$th HS snapshot can be expressed as

$$\mathbf{\Phi}_\mathrm{h}^k = \left(\sum_{i=0}^{L-1} (\mathbf{\Lambda}_{V_\mathrm{h}})^{iN_\mathrm{h}} [\mathrm{diag}(\mathbf{t}_\mathrm{h}^k), \mathbf{0}]^T \mathbf{I}_\mathrm{h} (\mathbf{\Lambda}_{N_\mathrm{h}^2 L})^{-iN_\mathrm{h}^2}\right)\mathbf{B} \quad (6)$$

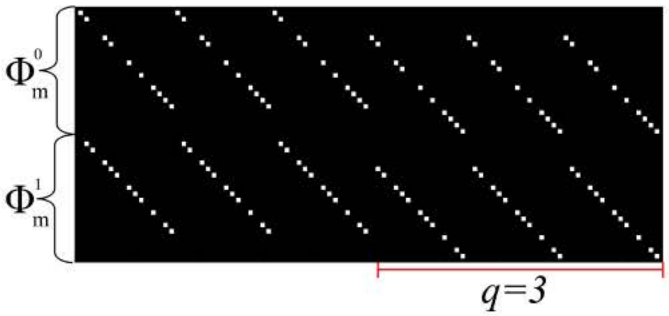

Fig. 7. MS CASSI measurement matrix $\mathbf{\Phi}_\mathrm{m}$ for $L = 6$, $K_\mathrm{m} = 2$ and $q = 3$.

where $N_\mathrm{h} = N/p$, $V_\mathrm{h} = N_\mathrm{h}(N_\mathrm{h} + L - 1)$, $\mathbf{t}_\mathrm{h}^k$ is the vectorized coded aperture ${\mathbf{T}_\mathrm{h}}^k$ of the HS imager, $\mathrm{diag}(\mathbf{t}_\mathrm{h}^k) \in \mathbb{R}^{N_\mathrm{h}^2 \times N_\mathrm{h}^2}$, $\mathbf{0}$ is the $N_\mathrm{h}^2 \times N_\mathrm{h}(L-1)$ zero matrix, $\mathbf{I}_\mathrm{h} = [\mathbf{I}, \mathbf{0}_\mathrm{h}]$, $\mathbf{I} \in \mathbb{R}^{N_\mathrm{h}^2 \times N_\mathrm{h}^2}$ is the identity matrix, and $\mathbf{0}_\mathrm{h}$ is the $N_\mathrm{h}^2 \times N_\mathrm{h}^2(L-1)$ zero matrix. Equivalently, (6) can be rewritten

$$\mathbf{\Phi}_\mathrm{h}^k = \sum_{i=0}^{L-1} (\mathbf{\Lambda}_{V_\mathrm{h}})^{iN_\mathrm{h}} [\mathrm{diag}(\mathbf{t}_\mathrm{h}^k), \mathbf{0}]^T \mathbf{B}_2 \mathbf{I}_\mathrm{C} (\mathbf{\Lambda}_{N^2 L})^{-iN^2} \quad (7)$$

where $\mathbf{B}_2 \in \mathbb{R}^{N_\mathrm{h}^2 \times N^2}$ is a spatial decimation operator. More specifically, the entries of the matrix $\mathbf{\Phi}_\mathrm{h}^k$ are defined as

$$\left(\mathbf{\Phi}_\mathrm{h}^k\right)_{ij} = \begin{cases} \left(t_\mathrm{h}^k\right)_{a_j + N_\mathrm{h} b_j + N_\mathrm{h}^2 c_j} & \text{if } i = a_j + N_\mathrm{h}(b_j + c_j) \\ 0 & \text{otherwise} \end{cases} \quad (8)$$

where $a_j = \lfloor \frac{j}{p} \rfloor$, $b_j = \lfloor \frac{j}{pN} \rfloor - \lfloor \frac{j}{N} \rfloor$, $c_j = \lfloor \frac{j}{N^2} \rfloor$ and $\lfloor . \rfloor$ denotes the integer part. Note that the matrix $\mathbf{\Phi}_\mathrm{h}^k$ is fully characterized by the vector $\mathbf{t}_\mathrm{h}^k$.

Similarly, Fig. 7 shows the structure of the CASSI measurement matrix $\mathbf{\Phi}_\mathrm{m}$ for the MS measurements. Note that each row of this matrix performs a linear combination between the pixels of the $q$ adjacent bands, which means that the spectral resolution of the MS sensor is $q$ times smaller than the one of the reference scene (e.g., $q = 4$ in Fig. 7). The matrix $\mathbf{\Phi}_\mathrm{m}^k$ associated with the $k$th MS snapshot can be expressed as

$$\mathbf{\Phi}_\mathrm{m}^k = \left(\sum_{i=0}^{L_\mathrm{m}-1} (\mathbf{\Lambda}_V)^{iqN} [\mathrm{diag}(\mathbf{t}_\mathrm{m}^k), \mathbf{0}]^T \mathbf{I}_\mathrm{m} (\mathbf{\Lambda}_{N^2 L_\mathrm{m}})^{-iN^2}\right)\mathbf{L} \quad (9)$$

where $L_\mathrm{m} = L/q$, $\mathbf{t}_\mathrm{m}^k$ is the vectorized coded aperture $\mathbf{T}_\mathrm{m}^k$ of the MS imager, $\mathrm{diag}(\mathbf{t}_\mathrm{m}^k) \in \mathbb{R}^{N^2 \times N^2}$, $\mathbf{0}$ is the $N^2 \times N(L_\mathrm{m} - 1)$ zero matrix, $\mathbf{I}_\mathrm{m} = [\mathbf{I}, \mathbf{0}_\mathrm{m}]$, $\mathbf{I} \in \mathbb{R}^{N^2 \times N^2}$ is the identity matrix, and $\mathbf{0}_\mathrm{m}$ is the $N^2 \times N^2(L_\mathrm{m} - 1)$ zero matrix. Equivalently, (9) can be rewritten

$$\mathbf{\Phi}_\mathrm{m}^k = \sum_{i=0}^{L_\mathrm{m}-1} (\mathbf{\Lambda}_V)^{iqN} [\mathrm{diag}(\mathbf{t}_\mathrm{m}^k), \mathbf{0}]^T \mathbf{L}_2 \mathbf{I}_\mathrm{mC} (\mathbf{\Lambda}_{N^2 L})^{-iN^2 q} \quad (10)$$

where $\mathbf{L}_2 \in \mathbb{R}^{N^2 \times N^2 q}$ is a spatial decimation operator, and $\mathbf{I}_\mathrm{mC} = [\mathbf{I}, \mathbf{0}_\mathrm{mC}]$, $\mathbf{I} \in \mathbb{R}^{N^2 q \times N^2 q}$ is the identity matrix, and $\mathbf{0}_\mathrm{mC}$ is the $N^2 q \times N^2 q(L_\mathrm{m} - 1)$ zero matrix.

More precisely, the entries of the matrix $\mathbf{\Phi}_\mathrm{m}^k$ can be written as follows

$$\left(\mathbf{\Phi}_\mathrm{m}^k\right)_{ij} = \begin{cases} (\mathbf{t}_\mathrm{m}^k)_{i - r_j(N^2 - N)} & \text{if } i = j \bmod N^2 + Nj/(qN^2) \\ & \text{and } j - r_j N \geq 0 \\ 0 & \text{otherwise} \end{cases} \quad (11)$$

where $r_j = j/(N^2)$. Note that that the matrix $\mathbf{\Phi}_{\mathrm{m}}^k$ is fully characterized by the vector $\mathbf{t}_{\mathrm{m}}^k$.

### *B. Designing the Matrices $\mathbf{\Phi}_h$ and $\mathbf{\Phi}_m$*

In CS theory, a suitable measurement matrix $\mathbf{\Phi} = [\mathbf{\Phi}_{\mathrm{h}}^T, \mathbf{\Phi}_{\mathrm{m}}^T]^T$ is desired to be as incoherent as possible with the sparse dictionary $\mathbf{\Psi}$ [9]. The mutual coherence of the Gram matrix $\mathbf{G} = (\mathbf{\Phi\Psi})^T(\mathbf{\Phi\Psi})$ is defined as the off-diagonal entry in $\mathbf{G}$ with the largest absolute magnitude. As a consequence, we propose to optimize the sensing matrix by minimizing the mutual coherence of $\mathbf{G}$. Considering that the dictionary is known, a sensing matrix can be chosen such that the corresponding Gram matrix is as close as possible to the identity [23], i.e.,

$$\mathbf{G} = \mathbf{\Psi}^T\mathbf{\Phi}^T\mathbf{\Phi\Psi} \approx \mathbf{I}. \tag{12}$$

Note that if the dictionary $\mathbf{\Psi}$ is an orthogonal basis ($\mathbf{\Psi}^T\mathbf{\Psi} = \mathbf{I}$), in order to have (12), it make sense to choose $\mathbf{\Phi}$ such that $\mathbf{\Phi}^T\mathbf{\Phi} \approx \mathbf{I}$. Thus, the design of the sensing matrix reduces to an appropriate choice of $\mathbf{\Phi}$. The choice of an appropriate sensing matrix for CS has been investigated before (independently of the dictionary), e.g., in [8], [24], and [25]. In [24], an approach for making the matrices associated with the different snapshots as complementary as possible was investigated. We propose to apply this concept to our problem to choose the matrix $\mathbf{\Phi}$ as a binary matrix containing only one 1 per column. Denote as $\boldsymbol{c} = [c_0, \cdots, c_{N^2L-1}]^T$ the vector such that

$$c_j = \sum_{i=0}^{K_{\mathrm{h}}V_{\mathrm{h}}-1} (\mathbf{\Phi}_{\mathrm{h}})_{i,j} + \sum_{i=0}^{K_{\mathrm{m}}V_{\mathrm{m}}-1} (\mathbf{\Phi}_{\mathrm{m}})_{i,j} \tag{13}$$

where $c_j$ corresponds to the number of ones in the $j$th column of $\mathbf{\Phi}$. Note that $j = 0, ..., N^2L-1$ where $N^2L$ is the number of columns of the matrix $\mathbf{\Phi}$, and that $(\mathbf{\Phi}_{\mathrm{h}})_{i,j}$ and $(\mathbf{\Phi}_{\mathrm{m}})_{i,j}$ are the elements of the $i$th row and $j$th column of the sensing matrices $\mathbf{\Phi}_{\mathrm{h}}$ and $\mathbf{\Phi}_{\mathrm{m}}$, respectively. When each column of $\mathbf{\Phi}$ contains exactly one 1 and all other values are 0, the matrix $\mathbf{\Phi}$ satisfies the following relations

$$\sigma_c^2 = \frac{1}{N^2L}\sum_{j=0}^{N^2L-1}(c_j - \overline{c})^2 = 0, \quad \overline{c} = 1. \tag{14}$$

Since these conditions are too restrictive in practice, we propose to design the matrix $\mathbf{\Phi}$ by minimizing the variance $\sigma_c^2$ with the constraint $\overline{c} = 1$. Since the entries of $\boldsymbol{c}$ are binary, this problem can be solved using the direct binary search algorithm for generating the patterns $\mathbf{T}^k$ (see [24] for more details). Finally, it is worth noting that the design of the matrix $\mathbf{\Phi}$ takes into account two different systems (with different spatial and spectral resolutions), which has (to the best of our knowledge) never been addressed in CS imaging.

## IV. FUSING COMPRESSED HS AND MS IMAGES USING A REGULARIZED INVERSE PROBLEM

### *A. Problem Formulation*

The fusion strategy adopted in this work is based on the following inverse problem

$$\widehat{\boldsymbol{f}} = \arg\min_{\mathbf{f}} \frac{1}{2}||\mathbf{\Phi}_{\mathrm{h}}\mathbf{f} - \tilde{\mathbf{y}}_{\mathrm{h}}||_2^2 + \frac{1}{2}||\mathbf{\Phi}_{\mathrm{m}}\mathbf{f} - \tilde{\mathbf{y}}_{\mathrm{m}}||_2^2 + \phi(\mathbf{f}) \tag{15}$$

where the two first terms are the data fidelity terms associated with the HS and MS observations, $||\cdot||_2$ is the $l_2$ norm and the last term ensures an appropriate regularization. In order to build the regularization term, we decompose the vectorized image $\boldsymbol{f}$ onto a basis $\mathbf{\Psi} \in \mathbb{R}^{N^2L\times N^2L}$ in order to obtain a sparse representation. Denoting as $\mathbf{x} \in \mathbb{R}^{N^2L}$ the vector containing the coefficients of $\mathbf{f}$ in this basis, we introduce the following regularization term

$$\phi(\mathbf{f}) = \lambda_1||\mathbf{\Psi}^T\mathbf{f}||_1 + \lambda_2||\mathcal{L}\mathbf{f}||_1 \tag{16}$$

which attempts to preserve the sparsity of the vector $\mathbf{x} = \mathbf{\Psi}^T\mathbf{f}$ in the domain of the representation basis $\Psi$, and the smoothness of $\mathbf{f}$ in the spatial domain via the operator $\mathcal{L}$, which enforces piecewise constant solutions and is associated with the $TV$ regularizer (see [26] for more details). Note that $||\cdot||_1$ is the $l_1$ norm and that $\lambda_1$, $\lambda_2$ are two regularization parameters.

### *B. Proposed ADMM*

The direct resolution of problem (15) involves the inversion of large matrices, which requires a too high computational cost. To decouple the original problem into smaller subproblems, we introduce the following notations

$$\begin{aligned}\mathbf{\Phi}_{\mathrm{h}} &= [\left(\mathbf{\Phi}_{\mathrm{h}}^1\right)^T, \cdots, \left(\mathbf{\Phi}_{\mathrm{h}}^{K_{\mathrm{h}}}\right)^T]^T,\\ \mathbf{\Phi}_{\mathrm{m}} &= [\left(\mathbf{\Phi}_{\mathrm{m}}^1\right)^T, \cdots, \left(\mathbf{\Phi}_{\mathrm{m}}^{K_{\mathrm{m}}}\right)^T]^T,\\ \tilde{\mathbf{y}} &= [\tilde{\mathbf{y}}_{\mathrm{h}}^T, \tilde{\mathbf{y}}_{\mathrm{m}}^T]^T\end{aligned} \tag{17}$$

where $\tilde{\mathbf{y}}_{\mathrm{h}}$, and $\tilde{\mathbf{y}}_{\mathrm{m}}$ are the measurement matrices and vectors associated with the $k_{\mathrm{h}}$th and $k_{\mathrm{m}}$th snapshots for the HS and MS imagers, respectively. This decomposition allows us to obtain $K = K_{\mathrm{h}} + K_{\mathrm{m}}$ simpler problems with respect to (w.r.t.) $\mathbf{f}$, where $K$ is the total number of snapshots. More precisely, we propose an alternative way to solve (15) with the regularizer (16) by splitting the objective function as follows

$$\begin{aligned}&\underset{\boldsymbol{v}_\alpha,\boldsymbol{u},\boldsymbol{v}}{\text{minimize}} \quad f(\boldsymbol{v}_\alpha, \boldsymbol{u}, \boldsymbol{v})\\ &\text{subject to } \boldsymbol{v}_\alpha = \mathbf{f} \text{ for } \alpha = 1, \cdots, K_{\mathrm{h}}, \cdots, K\\ &\qquad\qquad \mathbf{f} = \mathbf{\Psi}\boldsymbol{u}\\ &\qquad\qquad \boldsymbol{v} = \mathcal{L}\mathbf{f}\end{aligned} \tag{18}$$

where

$$\begin{aligned}f(\boldsymbol{v}_\alpha, \boldsymbol{u}, \boldsymbol{v}) = &\frac{1}{2}\sum_{k_{\mathrm{h}}=1}^{K_{\mathrm{h}}}\left\|\mathbf{\Phi}_{\mathrm{h}}^{k_{\mathrm{h}}}\boldsymbol{v}_{k_{\mathrm{h}}} - \tilde{\mathbf{y}}_{\mathrm{h}}^{k_{\mathrm{h}}}\right\|_2^2\\ &+\frac{1}{2}\sum_{k_{\mathrm{m}}=1}^{K_{\mathrm{m}}}\left\|\mathbf{\Phi}_{\mathrm{m}}^{k_{\mathrm{m}}}\boldsymbol{v}_{K_{\mathrm{h}}+k_{\mathrm{m}}} - \tilde{\mathbf{y}}_{\mathrm{m}}^{k_{\mathrm{m}}}\right\|_2^2 + \psi(\boldsymbol{u}, \boldsymbol{v})\end{aligned} \tag{19}$$

with

$$\psi(\boldsymbol{u}, \boldsymbol{v}) = \lambda_1||\boldsymbol{u}||_1 + \lambda_2||\boldsymbol{v}||_1 \tag{20}$$

and where the summations in the two first terms are obtained after splitting the matrices $\mathbf{\Phi}_{\mathrm{h}}$ and $\mathbf{\Phi}_{\mathrm{m}}$ into $K_{\mathrm{h}}$ and $K_{\mathrm{m}}$ matrices associated with the different snapshots. Then the procedure consists of optimizing the objective function $f(\boldsymbol{v}_\alpha, \boldsymbol{u}, \boldsymbol{v})$ w.r.t. $\boldsymbol{v}_\alpha$, $\boldsymbol{u}$ and $\boldsymbol{v}$, which leads to Algorithm 1.

**Algorithm 1** ADMM Compressive Spectral Image Fusion

```
1: Input $\boldsymbol{\Phi}_{\text{h}}$, $\boldsymbol{\Phi}_{\text{m}}$, $\tilde{\mathbf{y}}$
2: Initialization $(\boldsymbol{\nu}, \boldsymbol{u}, \boldsymbol{v}, \mathbf{f}) = 0$
3: repeat
     % Optimize w.r.t $\boldsymbol{\nu}_\alpha$ (see Algorithm 2)
4:       $\boldsymbol{\nu}_\alpha^\ell = \underset{\boldsymbol{\nu}_\alpha}{\text{minimize}}\ f(\boldsymbol{\nu}_\alpha, \boldsymbol{u}^{\ell-1}, \boldsymbol{v}^{\ell-1})$
     % Optimize w.r.t $\boldsymbol{u}$ and $\boldsymbol{v}$ (see Algorithm 3)
5:       $(\boldsymbol{u}^\ell, \boldsymbol{v}^\ell) = \underset{(\boldsymbol{u},\boldsymbol{v})}{\text{minimize}}\ f(\boldsymbol{\nu}_\alpha^\ell, \boldsymbol{u}, \boldsymbol{v})$
     % Estimate $\mathbf{f}$ using (31)
6:       $\mathbf{f}^\ell \leftarrow$ solve (18) w.r.t. $\mathbf{f}$
     % update slack variables (see Algorithm 4)
7: until some stopping criterion is satisfied
8: return $\mathbf{f}^\ell$
```

**Algorithm 2**

```
Input $\boldsymbol{\Phi}_{\text{h}}$, $\boldsymbol{\Phi}_{\text{m}}$, $\tilde{\mathbf{y}}$
Initialization $(\boldsymbol{\nu}_{\text{h}}, \boldsymbol{\nu}_{\text{m}}, \mathbf{d}, \mathbf{f}) = 0$
repeat
    % updating $\boldsymbol{\nu}_{\text{h}}$
        $\boldsymbol{\nu}_{\text{h}}^\ell = \sum_{k_{\text{h}}=1}^{K_{\text{h}}} \left(\boldsymbol{\Phi}_{\text{h}}^{k_{\text{h}}T}\boldsymbol{\Phi}_{\text{h}}^{k_{\text{h}}} + \rho\mathbb{I}_{N^2L}\right)^{-1}$
              $\left(\rho\left(\mathbf{f}^{\ell-1} + \mathbf{d}_{k_{\text{h}}}^\ell\right) + \boldsymbol{\Phi}_{\text{h}}^{k_{\text{h}}T}\tilde{\mathbf{y}}_{\text{h}}^{k_{\text{h}}}\right)$
    % updating $\boldsymbol{\nu}_M$
        $\boldsymbol{\nu}_{\text{m}}^\ell = \sum_{k_{\text{m}}=1}^{K_{\text{m}}} \left(\boldsymbol{\Phi}_{\text{m}}^{k_{\text{m}}T}\boldsymbol{\Phi}_{\text{m}}^{k_{\text{m}}} + \rho\mathbb{I}_{N^2L}\right)^{-1}$
              $\left(\rho\left(\mathbf{f}^{\ell-1} + \mathbf{d}_{K_{\text{h}}+k_{\text{m}}}^\ell\right) + \boldsymbol{\Phi}_{\text{m}}^{k_{\text{m}}T}\tilde{\mathbf{y}}_{\text{m}}^{k_{\text{m}}}\right)$
until some stopping criterion is satisfied
return $\boldsymbol{\nu}_{\text{h}}^\ell$, $\boldsymbol{\nu}_{\text{m}}^\ell$
```

An approach for solving (18) is to minimize its augmented Lagrangian [27]. The Lagrangian and its optimization are studied independently in the next subsections.

*1) Optimization w.r.t. $\boldsymbol{\nu}_\alpha$:* Decomposing the vector $\upsilon$ as

$$\boldsymbol{\nu} = [\boldsymbol{\nu}_{\text{h}}^T, \boldsymbol{\nu}_{\text{m}}^T]^T \tag{21}$$

with $\boldsymbol{\nu}_{\text{h}} = [\boldsymbol{\nu}_1^T, \cdots, \boldsymbol{\nu}_{K_{\text{h}}}^T]^T$ and $\boldsymbol{\nu}_{\text{m}} = [\boldsymbol{\nu}_{K_{\text{h}}+1}^T, \cdots, \boldsymbol{\nu}_K^T]^T$, the minimizations w.r.t. the variables $\boldsymbol{\nu}_{\text{h}}$ and $\boldsymbol{\nu}_{\text{m}}$ can be conducted separately. For instance, when using the scaled form of the ADMM algorithm, the Lagrangian of (19) w.r.t. $\boldsymbol{\nu}_{\text{h}}$ is

$$L_{\text{h}}(\boldsymbol{\nu}_{\text{h}}) = \frac{1}{2}\sum_{k_{\text{h}}=1}^{K_{\text{h}}}\left\|\boldsymbol{\Phi}_{\text{h}}^{k_{\text{h}}}\boldsymbol{\nu}_{k_{\text{h}}} - \tilde{\mathbf{y}}_{\text{h}}^{k_{\text{h}}}\right\|_2^2 + \frac{\rho}{2}\sum_{k_{\text{h}}=1}^{K_{\text{h}}}\left\|\mathbf{f} - \boldsymbol{\nu}_{k_{\text{h}}} + \mathbf{d}_{k_{\text{h}}}\right\|_2^2 \tag{22}$$

where $\mathbf{d}_{k_{\text{h}}}$ is a slack variable. The update term for $\boldsymbol{\nu}_{\text{h}}$ can be obtained by differentiating (22) w.r.t. $\boldsymbol{\nu}_{\text{h}}$ and forcing it to be zero. Of course, the Lagrangian of $\boldsymbol{\nu}_{\text{m}}$ is similar to the Lagrangian of $\boldsymbol{\nu}_{\text{h}}$ and is obtained by replacing $\boldsymbol{\Phi}_{\text{h}}$ by $\boldsymbol{\Phi}_{\text{m}}$, $\boldsymbol{\nu}_{\text{h}}$ by $\boldsymbol{\nu}_{\text{m}}$, and $\tilde{\mathbf{y}}_{\text{h}}$ by $\tilde{\mathbf{y}}_{\text{m}}$. Algorithm 2 shows how $\boldsymbol{\nu}_{\text{h}}$ and $\boldsymbol{\nu}_{\text{m}}$ are updated from the minimization of their respectives Lagrangians. Note that the sparsity of the matrices $\boldsymbol{\Phi}_{\text{h}}$ and $\boldsymbol{\Phi}_{\text{m}}$ allows the matrices $\left(\boldsymbol{\Phi}_{\text{h}}^{k_{\text{h}}T}\boldsymbol{\Phi}_{\text{h}}^{k_{\text{h}}} + \rho\mathbb{I}_{N^2L}\right) \in \mathbb{R}^{N^2L\times N^2L}$ and $\left(\boldsymbol{\Phi}_{\text{m}}^{k_{\text{m}}T}\boldsymbol{\Phi}_{\text{m}}^{k_{\text{m}}} + \rho\mathbb{I}_{N^2L}\right) \in \mathbb{R}^{N^2L\times N^2L}$ (where $\mathbb{I}_{N^2L}$ is the $N^2L \times N^2L$ identity matrix) to be inverted with reasonable computational complexity. Note that the scaled and unscaled forms of the ADMM are equivalent. However, if one do not wish to emphasize the role of the dual variable, and use datasets with arbitrary size, it is more convenient to use the scaled form.

*2) Optimization w.r.t. $\boldsymbol{u}$:* Problem (15) can be rewritten

$$\begin{aligned}&\underset{\boldsymbol{\nu},\boldsymbol{u},\boldsymbol{v}}{\text{minimize}} \quad L_{\text{h}}(\boldsymbol{\nu}_{\text{h}}) + L_{\text{m}}(\boldsymbol{\nu}_{\text{m}}) + \lambda_1||\boldsymbol{u}||_1 + \lambda_2||\boldsymbol{v}||_1\\ &\text{subject to } \mathbf{f} = \boldsymbol{\Psi}\boldsymbol{u} \text{ and } \boldsymbol{v} = \boldsymbol{\mathcal{L}}\mathbf{f}.\end{aligned} \tag{23}$$

The minimization w.r.t. $\boldsymbol{u}$ can be solved by introducing auxiliary variables to split the data fidelity and regularization terms. More specifically, by introducing the splittings $\boldsymbol{u} = \boldsymbol{u}_0$ and $\boldsymbol{v} = \boldsymbol{v}_0$, (23) leads to

$$\begin{aligned}&\underset{\boldsymbol{\nu}_\alpha,\boldsymbol{u},\boldsymbol{v},\boldsymbol{u_0},\boldsymbol{v}_0}{\text{minimize}} \quad L_{\text{h}}(\boldsymbol{\nu}_{\text{h}}) + L_{\text{m}}(\boldsymbol{\nu}_{\text{m}}) + \lambda_1\|\boldsymbol{u}_0\|_1 + \lambda_2\|\boldsymbol{v}_0\|_1\\ &\text{subject to } \mathbf{f} = \boldsymbol{\Psi}\boldsymbol{u}, \boldsymbol{u} = \boldsymbol{u}_0, \boldsymbol{v} = \boldsymbol{\mathcal{L}}\mathbf{f}, \boldsymbol{v} = \boldsymbol{v}_0.\end{aligned} \tag{24}$$

Problem (24) can be solved by optimizing the Lagrangian w.r.t. all its variables. The optimization w.r.t. $\boldsymbol{u}_0$ reduces to

$$\underset{\boldsymbol{u}_0}{\text{minimize}} \quad L_0(\boldsymbol{u}_0) \tag{25}$$

where

$$L_0(\boldsymbol{u}_0) = \lambda_1\|\boldsymbol{u}_0\|_1 + \frac{\rho}{2}\left\|\boldsymbol{u} - \boldsymbol{u}_0 + \mathbf{d}_{(K+1)}\right\|_2^2. \tag{26}$$

The optimization w.r.t. $\boldsymbol{u}$ can be written

$$\underset{\boldsymbol{u}}{\text{minimize}} \quad L_u(\boldsymbol{u}) \tag{27}$$

with

$$L_u(\boldsymbol{u}) = \frac{\rho}{2}\left\|\boldsymbol{u} - \boldsymbol{u}_0 + \mathbf{d}_{(K+1)}\right\|_2^2 + \frac{\rho}{2}\left\|\mathbf{f} - \boldsymbol{\Psi}\boldsymbol{u} + \mathbf{d}_{(K+2)}\right\|_2^2 \tag{28}$$

where the variables $\mathbf{d}_k$ are slack variables. Of course, the optimizations w.r.t. $\boldsymbol{v}_0$ and $\boldsymbol{v}$ (in (24)) can be solved similarly. The Lagrangians $L_0(\boldsymbol{u}_0)$ and $L_0(\boldsymbol{v}_0)$ being non-differentiable, we update these parameters by using soft thresholding operations, which result from the computation of appropriate proximal operators (see [26], [27] for details). Algorithm 3 summarizes how each variable $\boldsymbol{u}$ and $\boldsymbol{v}$ can be updated from the minimization of their respective Lagrangians where

$$S_{\lambda/\rho}(x) = \begin{cases} x - \dfrac{\lambda}{\rho} & \text{if } x > \frac{\lambda}{\rho}\\ x + \dfrac{\lambda}{\rho} & \text{if } x < -\frac{\lambda}{\rho}\\ 0 & \text{otherwise}\end{cases} \tag{29}$$

*3) Estimating $\boldsymbol{f}$:* The final step is to estimate the unknown image $\mathbf{f}$ from (24) by minimizing its Lagrangian w.r.t. $\mathbf{f}$ defined as

$$\begin{aligned}L_f(\mathbf{f}) = \frac{\rho}{2}\Bigg(&\sum_{k=1}^{K}\|\mathbf{f} - \boldsymbol{\nu}_k + \mathbf{d}_k\|_2^2 + \left\|\mathbf{f} - \boldsymbol{\Psi}\boldsymbol{u}_0 + \mathbf{d}_{(K+2)}\right\|_2^2\\ &+ \left\|\mathbf{f} - \boldsymbol{v}_0 + \mathbf{d}_{(K+4)}\right\|_2^2\Bigg)\end{aligned} \tag{30}$$

where the first term directly results from $L_{\text{h}}(\boldsymbol{\nu}_{\text{h}})$ and $L_{\text{m}}(\boldsymbol{\nu}_{\text{m}})$ in (22), whereas the second and third terms from $L_u(\boldsymbol{u})$ and $L_\upsilon(\boldsymbol{v})$ in (28). The optimization of $L_f(\boldsymbol{f})$ can be performed by forcing its derivative to 0, which yields the update term of $\boldsymbol{f}$ in line 5 of Algorithm 1.

**Algorithm 3**

```
Input $\boldsymbol{\Psi}$, $\boldsymbol{\mathcal{L}}$
Initialization $(\boldsymbol{u}, \boldsymbol{v}, \mathbf{d}, \mathbf{f}, \boldsymbol{u}_0, \boldsymbol{v}_0) = 0$
repeat
    % updating $\boldsymbol{u}_0$
    $\boldsymbol{u}_0^\ell = S_{\lambda_1/\rho}(\boldsymbol{u}^{\ell-1} + \mathbf{d}_{K+1}^{\ell-1})$
    % updating $\boldsymbol{u}$
    $\boldsymbol{u}^\ell = \left(\boldsymbol{\Psi}^T\boldsymbol{\Psi} + \mathbb{I}_{N^2L}\right)^{-1} \left(\boldsymbol{\Psi}\left(\mathbf{f}^{\ell-1} + \mathbf{d}_{(K+2)}^{\ell-1}\right) + \boldsymbol{u}_0^\ell - \mathbf{d}_{(K+1)}^{\ell-1}\right)$
    % updating $\boldsymbol{v}_0$
    $\boldsymbol{v}_0^\ell = S_{\lambda_2/\rho}(\boldsymbol{v}^{\ell-1} + \mathbf{d}_{K+3}^{\ell-1}))$
    % updating $\boldsymbol{v}$
    $\boldsymbol{v}^\ell = \left(\mathcal{L}^T\mathcal{L} + \mathbb{I}_{N^2L}\right)^{-1} \left(\mathcal{L}\left(\mathbf{f}^{\ell-1} + \mathbf{d}_{(K+4)}^{\ell-1}\right) + \boldsymbol{v}_0^\ell + \mathbf{d}_{(K+3)}^{\ell-1}\right)$
until some stopping criterion is satisfied
return $\boldsymbol{u}^\ell$, $\boldsymbol{\nu}^\ell$
```

**Algorithm 4**

```
% updating slack variables
$\mathbf{d}_{k_\mathrm{h}}^\ell = \mathbf{f}^\ell - \boldsymbol{\nu}_{k_\mathrm{h}}^\ell + \mathbf{d}_{k_\mathrm{h}}^{\ell-1}$
$\mathbf{d}_{K_\mathrm{h}+k_\mathrm{m}}^\ell = \mathbf{f}^\ell - \boldsymbol{\nu}_{K_\mathrm{h}+k_\mathrm{m}}^\ell + \mathbf{d}_{K_\mathrm{h}+k_\mathrm{m}}^{\ell-1}$
$\mathbf{d}_{(K+1)}^\ell = \boldsymbol{u}^\ell - \boldsymbol{u}_0^\ell + \mathbf{d}_{K+1}^{\ell-1}$
$\mathbf{d}_{(K+2)}^\ell = \mathbf{f}^\ell - \boldsymbol{\Psi}\boldsymbol{u}_0^\ell + \mathbf{d}_{(K+2)}^{\ell-1}$
$\mathbf{d}_{(K+3)}^\ell = \boldsymbol{v}^\ell - \boldsymbol{v}_0^\ell + \mathbf{d}_{(K+3)}^{\ell-1}$
$\mathbf{d}_{(K+4)}^\ell = \mathbf{f}^\ell - \boldsymbol{\Psi}\boldsymbol{v}^\ell + \mathbf{d}_{(K+4)}^{\ell-1}$
```

*4) Slack Variables:* The slack variables in **d** have also to be updated. We propose to update them using the procedure considered in [27] for the Lasso problem. Algorithm 4 summarizes the different steps for this update.

*5) Convergence:* The problem solved in this paper is a convex relaxation of the CS problem. Since the functions $f$ and $\phi$ are convex, the subproblems corresponding to the update of each variable are convex and have a unique solution. As a consequence, there exist a unique image **f** that minimizes the augmented Lagrangian. Indeed, if we introduce the vector $\mathbf{z} = [\boldsymbol{\nu}_1^T, \cdots, \boldsymbol{\nu}_K^T, \boldsymbol{u}^T, \boldsymbol{v}^T]^T$ and the matrix $\mathbf{M} = [\mathbf{I}, \cdots, \mathbf{I}, \boldsymbol{\Psi}, \boldsymbol{\mathcal{L}}^T]^T$, we can rewrite problem (18) as the minimization of $f(\mathbf{z})$, subject to the constraint $\mathbf{Mf} = \mathbf{z}$. Given that the function $f$ is closed, proper and convex and the matrix **M** is full column rank, from Theorem 8 in [37], we know that the sequence of iterates $\{\mathbf{f}^l\}$ generated by Algorithm 1 converges to a solution of (15).

## V. SIMULATION RESULTS

### A. Simulation Scenario

Two imagers were considered in each experiment to generate the low spatial/high spectral and high spatial/low spectral resolution measurements $\tilde{\mathbf{y}}_\mathrm{h}$ and $\tilde{\mathbf{y}}_\mathrm{m}$. Both systems used the same high-resolution image, which was degraded using spatial and spectral degradations and compressed. The matrices $\boldsymbol{\Phi}_\mathrm{h}$ and $\boldsymbol{\Phi}_\mathrm{m}$ were generated as described in Section III. The reference image considered in this work is mainly the classical ROSIS image acquired over Pavia, northern Italy [28] reduced to 256 × 256 pixels and 92 bands. The HS datacube was obtained by applying a 5 × 5 Gaussian lowpass filter in each band and by using a 4:1 decimation ratio ($p = 2$). Similarly, the MS data was generated by using a 4:1 decimation ratio ($q = 4$). Algorithm 1 was then used to estimate the image **f**. The main parameters were obtained as follows

- The values of $\lambda_1$ and $\lambda_2$ were selected by cross-validation and we found that $\lambda_1 = \lambda_2 = 5 \times 10^{-4}$ provides good reconstruction results.
- The parameter $\rho$ was initialized close to zero and was updated as will be explained in Section V-B.
- The dictionary $\boldsymbol{\Psi}$ was selected as the Kronecker product $\mathbf{W} \otimes \mathbf{D}$, where **W** is a Symlet wavelet kernel, and **D** is a DCT operator. This choice is motivated by the fact that it has provided good image reconstruction results in previous works [8].
- The operator $\boldsymbol{\mathcal{L}}$ was decoupled in two operators acting on the rows and columns of each spectral band, as explained in [29].
- The stopping criterion was selected as in many ADMM algorithms [27]. More precisely, tolerances were introduced as $||\mathbf{f}^\ell - \boldsymbol{\nu}^\ell||_2 \leq \epsilon_1$ and $||\boldsymbol{\nu}^{\ell-1} - \boldsymbol{\nu}^\ell||_2 \leq \epsilon_2$ with $\epsilon_1 \leq 10^{-2}, \epsilon_2 \leq 10^{-4}$. In general, these stopping rules are satisfied before 30 iterations.
- The amount of data for the simulations was defined as the compression ratio, which expresses the amount of data in the measurement vectors with respect to number of elements in the reference image, that is Compression Ratio $= (K_\mathrm{h}V_\mathrm{h} + K_\mathrm{m}V_\mathrm{m}) / (N_\mathrm{h}^2 L + N^2 L_\mathrm{m})$

### B. How to Update Parameters $\lambda_1$, $\lambda_2$ and $\rho$?

The proposed algorithm requires to adjust three parameters, i.e., $\lambda_1$, $\lambda_2$ and $\rho$. The two first parameters $\lambda_1$ and $\lambda_2$ are related with the regularization terms of the proposed optimization problem. They were chosen by cross-validation for any dataset in order to obtain the best performance (as classically done for this kind of problem).

The fusion results also depend on the parameter $\rho$ appearing in the augmented Lagrangian (e.g., see (22)). In this work, this parameter was adjusted using the following rule

$$\rho^{\ell+1} = \begin{cases} \tau_l \rho^\ell & \text{if } ||\mathbf{f}^\ell - \boldsymbol{\nu}^\ell||_2 > \mu||\boldsymbol{\nu}^{\ell-1} - \boldsymbol{\nu}^\ell||_2 \\ \rho^\ell \tau_r & \text{if } ||\boldsymbol{\nu}^{\ell-1} - \boldsymbol{\nu}^\ell||_2 > \mu||\mathbf{f}^\ell - \boldsymbol{\nu}^\ell||_2 \\ \rho^\ell & \text{otherwise} \end{cases} \qquad (31)$$

where $\tau_l = \tau_r = 2$, $\mu = 10$ are common choices [27]. In practice, we have observed that it was sufficient to update $\rho$ every 10 iterations of the algorithm, as suggested in [27]. The main motivation behind this update rule is to try to keep the primal and dual residual norms within a factor of $\mu$ of one another as they both converge to zero [27].

### C. Fusion Quality Metrics

The metrics used to evaluate the quality of the proposed fusion strategy are summarized and explained below

- *RMSE:* The root mean square error (RMSE) is a similarity measure between the target image **f** and the fused image

$\hat{\mathbf{f}}$ defined as $\mathrm{RMSE}(\mathbf{f},\hat{\mathbf{f}}) = \frac{1}{N^2L}\|\mathbf{f}-\hat{\mathbf{f}}\|_2^2$. The smaller RMSE, the better the fusion quality.

- *UIQI:* The universal image quality index (UIQI) was proposed in [30] for evaluating the similarity between two single band images. It is related to the correlation, luminance distortion and contrast distortion of the estimated image w.r.t. the reference image. The UIQI between two single-band images $\mathbf{a} = [a_1, \cdots, a_N]$ and $\hat{\mathbf{a}} = [\hat{a}_1, \cdots, \hat{a}_N]$ is defined

$$\mathrm{UIQI}(\mathbf{a},\hat{\mathbf{a}}) = \frac{4\sigma_{a\hat{a}^2}\mu_a\mu_{\hat{a}}}{(\sigma_a^2+\sigma_{\hat{a}}^2)(\mu_a^2+\mu_{\hat{a}}^2)} \tag{32}$$

  where $(\mu_a, \mu_{\hat{a}}, \sigma_a^2, \sigma_{\hat{a}}^2)$ are the sample means and variances of $a$ and $\hat{a}$, and $\sigma_{a\hat{a}^2}$ is the sample covariance of $(a,\hat{a})$. The range of UIQI is $[-1,1]$ and $\mathrm{UIQI}(\mathbf{a},\hat{\mathbf{a}}) = 1$ when $\mathbf{a} = \hat{\mathbf{a}}$. For multi-band images, the overall UIQI is computed by averaging the UIQIs associated with the different bands.
- *SAM:* The spectral angle mapper (SAM) measures the spectral distortion between the actual and estimated images. The SAM of two spectral vectors $\mathbf{x}$ and $\hat{\mathbf{x}}$ is defined as $\mathrm{SAM}(\mathbf{x},\hat{\mathbf{x}}) = \arccos\left(\langle\mathbf{x},\hat{\mathbf{x}}\rangle/\|\mathbf{x}\|_2\|\hat{\mathbf{x}}\|_2\right)$. The overall SAM is finally obtained by averaging the SAMs computed from all image pixels. Note that the value of SAM is expressed in degrees and thus belongs to $(-90, 90]$. The smaller the absolute value of SAM, the less important the spectral distortion.
- *ERGAS:* The relative dimensionless global error in synthesis (ERGAS) calculates the amount of spectral distortion in the image [31]. It is defined as

$$\mathrm{ERGAS} = 100\frac{N^2L_{\mathrm{m}}}{N_{\mathrm{h}}^2L}\sqrt{\frac{1}{L}\sum_{i=0}^{L-1}\left(\frac{\mathrm{RMSE(i)}}{\mu_i}\right)^2} \tag{33}$$

  where $N^2L_{\mathrm{m}}/N_{\mathrm{h}}^2L$ is the ratio between the pixel sizes of the MS ans HS images, $\mu_i$ is the mean of the $i$th band of the HS image, and $L$ is the number of HS bands. The smaller ERGAS, the smaller the spectral distortion.
- *DD:* The degree of distortion (DD) between two images is defined as $\mathrm{DD}(\mathbf{f},\hat{\mathbf{f}}) = \frac{1}{N^2L}\|\mathbf{f}-\hat{\mathbf{f}}\|_1$. The smaller DD, the better the fusion.

### D. Fusion Results

The first simulation results displayed in Fig. 8 show the reconstructed image obtained with the proposed fusion method for a compression ratio of 0.4, which can be compared to the ground truth and the reconstruction obtained without CS. These results are compared with other fusion methods designed for compressed measurements [32] or for non-compressed data [14], [33].[1] The method studied in [14] referred to as "Sparse fusion" exploits the fact that HS images live in a low dimensional subspace defined by the endmembers whereas the method of [32] is based on a multi-resolution analysis and a simple maximum selection fusion rule. The method of [33] is adapted to multiple multi-focus images. It is based on a sparse model and formulates the fusion problem as an inverse-problem regularized with a cosparsity prior in order to estimate an all-in-focus image. Since the methods of [32] and [33] require the images to have the same size, the MS and HS images were interpolated to have the same size before applying these methods. Note that the images displayed

Fig. 8. Fusion results for the Pavia dataset (compression ratio of 0.4). (Top-Left) Groundtruth. (Top-Right) Hyperspectral/low spatial resolution image. (Second line-Left) Multispectral/low spectral resolution image. Reconstructed images using different methods: (Second line-Right) [32] (PSNR = 28 dB), (Third line-Left) [33] (PSNR = 36.99 dB), (Third line-Right) CASSI (PSNR = 32 dB), (Fourth line-Left) SSCSI (PSNR = 38 dB), (Fourth line-Right) Gaussian sensing matrix (PSNR = 41 dB), (Bottom) Sparse fusion [14] (PSNR = 42 dB).

---

[1] The authors are very grateful to A. Achim and S. Vorobyov who sent us their Matlab codes allowing a fair comparison.

TABLE I

PERFORMANCE OF DIFFERENT MS + HS FUSION METHODS (PAVIA DATA SET): RMSE ($\times 10^{-2}$), UIQI, SAM (DEGREES), ERGAS, DD ($\times 10^{-3}$), TIME (SECONDS) AND THE AMOUNT OF DATA (%)

| Methods | RMSE | UIQI | SAM | ERGAS | DD | time | data |
|---|---|---|---|---|---|---|---|
| Sparse | **1,092** | 0,986 | 1,588 | **1,055** | **0,712** | 98.0 | 100% |
| [33] | 3,122 | **0,990** | 3,555 | 1,940 | 1,521 | **56.8** | 100% |
| [32] | 4,562 | 0,887 | 6,214 | 4,935 | 2,401 | 6900 | 50% |
| Gaussian | 1,286 | **0,990** | **1,210** | 1,179 | 0,836 | 90.0 | **40%** |
| CASSI | 1,157 | 0,987 | 1,641 | 1,605 | 0,809 | 102 | **40%** |
| SSCSI | 1,406 | 0,995 | 1,394 | 1,607 | 0,893 | 120 | **40%** |

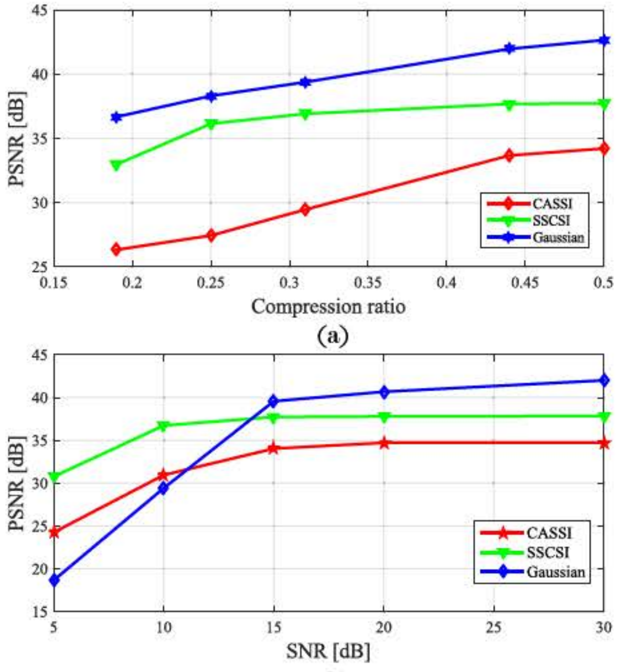

(a)

(b)

Fig. 9. PSNRs obtained with the proposed fusion method using CASSI, SSCSI and Gaussian sensing matrices for (a) different compression ratios (b) different SNR values.

in Fig. 8 were obtained from the red, green and blue bands of the spectral datacubes.

In order to complement our qualitative results, we compare the proposed fusion method with its sparse counterpart without any CS using quantitative measures. The simulation scenario was established as in [14]. Table I shows the quantitative metrics RMSE, SAM, UIQI, ERGAS and DD that were defined in Section V C. This comparison allows us to appreciate the differences between the different reconstructions in presence or absence of CS. We can conclude that the proposed approach provides competitive results, even if it is applied on a significantly reduced number of data samples.

## *E. Impact of the Sensing Matrix*

Several experiments were performed to test the impact of the sensing matrix on the reconstructed images. A Gaussian sensing matrix was used as a theoretical reference and compared to the other reconstructions in terms of PSNR. We are using the Gaussian matrix as a reference because it exhibits a very low coherence with any fixed representation, which is a desirable property for the success of data recovery [9]. However, note that there is currently no device allowing this kind of sampling to be implemented practically. Fig. 9(a) shows the reconstruction results (in terms of PSNR) obtained for the different matrices as a function of the amount of data expressed as a function of the compression ratio. The results obtained with Gaussian sensing matrices are better than those obtained using other matrices, as expected. Note that the PSNR values are directly proportional to the image size and to the execution time, which can be adjusted to reach a particular value for a given application. Similar results obtained with noisy images with different signal to noise ratios (SNRs) are displayed in Fig. 9(b). Note that an additive Gaussian noise was used in all experiments. Despite the loss in reconstruction quality, the proposed fusion approach provides a PSNR close to 40 dB for a noise level satisfying SNR $\geq$ 15 dB, which is very promising. Note that the performance of the different systems in presence of noise is better for CASSI and SSCSI than for the Gaussian matrix for low SNR values.

The next experiments compare the reconstruction results obtained using the optimized sensing matrix derived in Section III-B and more traditional random matrices. The optimized sensing matrix allows a more incoherent measurement matrix to be obtained than random realizations, which can lead to an improved reconstructed image. Fig. 10(a) shows the reconstruction results in terms of PSNR for the proposed approach with designed and random sensing matrices for the CASSI system with different compression ratios. From these results, we can conclude that the designed sensing matrix provides better results than random entries, as expected. Note that the results obtained with the optimized sensing matrix are close to those obtained by using other methods with incoherent CS matrices, such as Gaussian matrices. Similar results obtained with the SSCSI system are displayed in Fig. 10(b). Finally, it is interesting to mention that reconstructed images obtained for different compression ratios and levels of SNR are available in the technical report [34].

## *F. Motivations for Fusing HS and MS Images*

In order to illustrate the motivation for fusing HS and MS images, we have experimentally compared three reconstruction methods for the Pavia dataset using (1) $\tilde{\mathbf{y}}_{\mathrm{h}}$ only, (2) $\tilde{\mathbf{y}}_{\mathrm{m}}$ only and (3) $\tilde{\mathbf{y}}_{\mathrm{m}}$ and $\tilde{\mathbf{y}}_{\mathrm{h}}$ (proposed method). Quantitative results in terms of PSNR are reported in Table II showing the advantage of the proposed joint reconstruction method. For this experiments all the measurements has been simulated with the CASSI system with a compression ratio of 0.4. When we use the compressed HS image $\tilde{\mathbf{y}}_{\mathrm{h}}$ only, the spectral signatures are estimated accurately at the price of a degraded spatial resolution. Conversely, when the reconstruction is performed using the compressed MS image $\tilde{\mathbf{y}}_{\mathrm{m}}$ only, the spatial resolution of the reconstructed image is good with a degraded spectral signature. Combining the two measurements allows a good compromise in terms of spatial and spectral resolutions to be obtained. Fig. 11 shows the spectral signatures of a

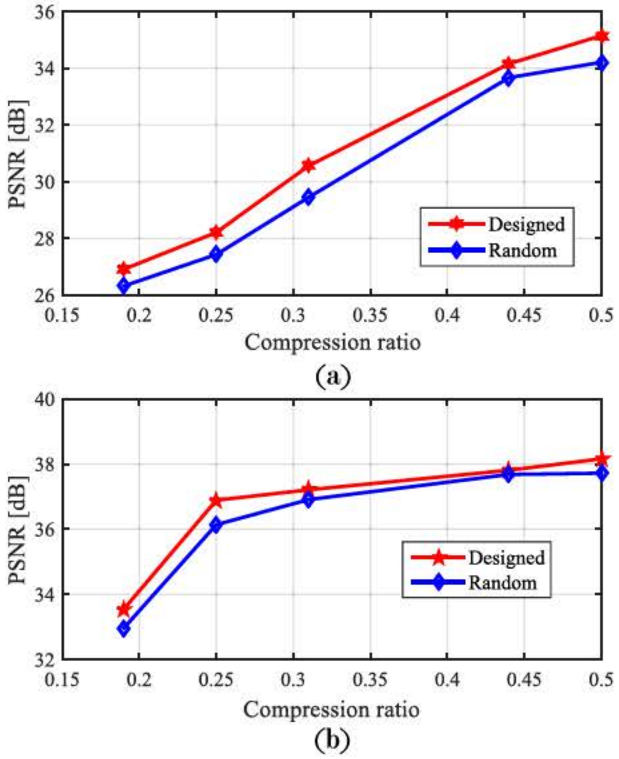

Fig. 10. PSNR comparison for the proposed fusion approach using random and designed random matrices with different compression ratios for (a) the CASSI system (b) the SSCSI system.

TABLE II

PSNR (dB) OF THE RECONSTRUCTED IMAGE USING SCENARIOS (1), (2), AND (3) (PAVIA DATASET)

| Scenario | PSNR [dB] |
|---|---|
| (1) | 27,79 |
| (2) | 31,46 |
| (3) | **34,45** |

reconstructed pixel using the three methods confirming this conclusion.

### *G. Test With Another Dataset*

This section presents some results obtained with the proposed fusion method applied to another dataset. The reference image is the high spatio-spectral image acquired over Moffett Field, CA, in 2009 by the JPL/NASA airborne visible/infrared imaging spectrometer (AVIRIS) [35]. This image was reduced to $256 \times 256$ pixels and 128 bands. Fig. 13 shows the RGB images (constructed from the red, green and blue bands of the spectral images) that result for the proposed fusion method for a compression ratio of 0.4 using different sensing matrices, which can be compared to the reconstruction obtained by using the Sparse Fusion method. Note that the reconstructed images are close to the groundtruth. The reader is invited to consult the technical report [34] for additional simulation results performed on two other datasets.

### *H. Algorithm Convergence*

Even though the convergence of Algorithm 1 can be proved, an exact recovery of the image $\mathbf{f}$ depends on its sparsity in the basis $\mathbf{\Psi}$ and the number of considered measurements (number of snapshots) due to the ill-posedness of the reconstruction problem. In order to show the good convergence of the proposed optimization algorithm, we are displaying in Fig. 12 the evolution of the cost function versus the number of iterations, showing that 20 iterations are sufficient to ensure a good reconstruction. This kind of result has been observed in all our experiments.

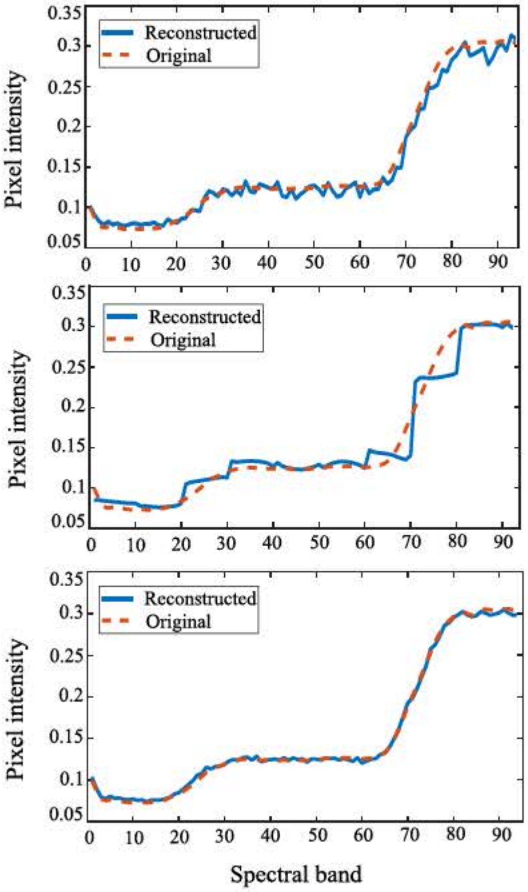

Fig. 11. Original and reconstructed spectral signature of pixel (121,4) using (Top) $\bar{\mathbf{y}}_{\mathrm{h}}$ only, (Middle) $\bar{\mathbf{y}}_{\mathrm{m}}$ only (Bottom) Jointly $\bar{\mathbf{y}}_{\mathrm{h}}$ and $\bar{\mathbf{y}}_{\mathrm{m}}$.

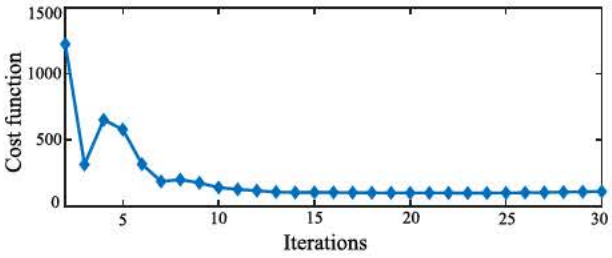

Fig. 12. Variations of the proposed cost function versus the number of iterations.

### *I. Computational Complexity Analysis*

The number of operations per iteration in Algorithm 1 depends on the underlying image size and the number of spectral bands. In particular, the computational complexity of Algorithm 2 is proportional to the number of nonzero

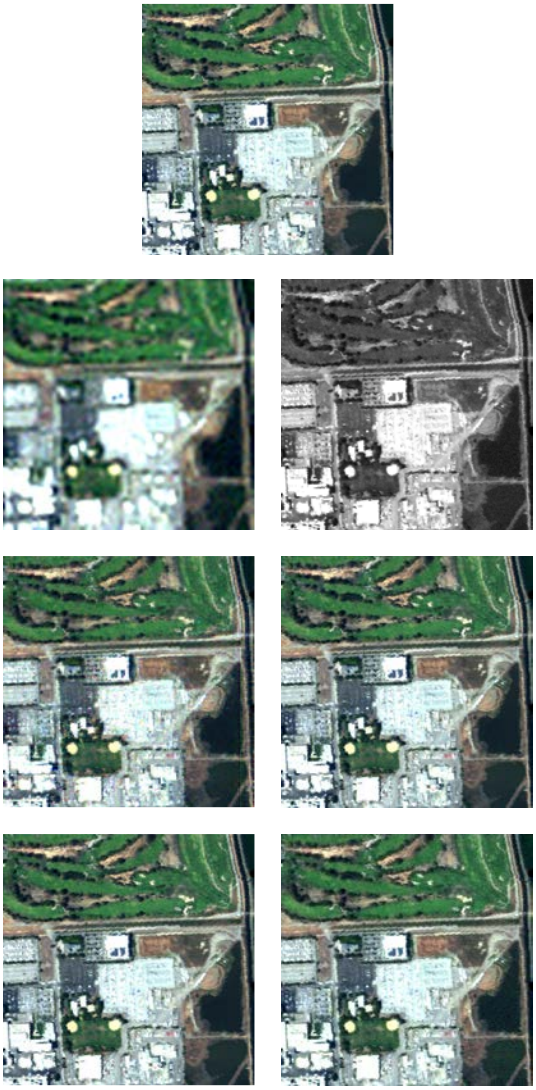

Fig. 13. Spatial fusion results for the Moffett Field dataset. (Top) Groundtruth. (Left-2) Hyperspectral/low spatial resolution image. (Right-2) Multispectral/low spectral resolution image. (Left-3) CASSI Reconstruction with the proposed fusion method (PSRN = 30 dB). (Right-3) SSCSI Reconstruction with the proposed fusion method (PSNR = 37 dB). (Left-4) Gaussian reconstruction with the proposed fusion method (PSNR = 42 dB). (Right-4) Sparse fusion (PSNR = 43 dB).

elements of the matrix $\boldsymbol{\Phi}^T\boldsymbol{\Phi}+\rho\mathbb{I}_{N^2L}$, with $\boldsymbol{\Phi}\in\mathbb{R}^{m\times n}$. The sparsity of this matrix can be exploited for its inversion by using efficient matrix factorizations and backsolve routines (e.g., Cholesky factorization [27], [35]). In this case, this operation can be carried out with $O(nm^2)$ operations plus the cost of forming the matrix $\boldsymbol{\Phi}^T\boldsymbol{\Phi}+\rho\mathbb{I}_{N^2L}$. The computational complexity of Algorithm 3 is known to be O($N^2L$). Note that the matrix inversions have to be computed at each time $\rho$ is updated. Thus, the total complexity of Algorithm 1 is O($N^2L(K_\mathrm{h}V_\mathrm{h}+K_\mathrm{m}V_\mathrm{m})^2$).

## VI. CONCLUSION

This work showed that compressive projections can be used to fuse high spectral/low spatial and high spatial/low spectral resolution images without the need of expensive image reconstruction methods. The image fusion problem was formulated as an inverse problem with two data fidelity terms related to the images to be fused and two regularizations ensuring a smooth reconstructed image a sparse decomposition of the image in an appropriate dictionary. An ADMM algorithm was studied for solving this inverse problem. Our experiments showed that algorithms based on compressed sensing can recover images with high spatial and spectral resolutions using as few as 50% of the data with PSNRs larger than 40dB, which is comparable with results obtained with other fusion approaches processing images without compressed sensing. The main advantage of the proposed fusion rule is the reduced amount of data required to estimate the target multi-band image yielding a reconstruction performance close to the one obtained with other fusion methods designed without compressed sensing. Future work includes the study of methods allowing the hyperparameters to be automatically estimated from the data, as the ones presented in [36]. In this work, the sensing matrices have been optimized considering the compressed sensing architecture only (i.e., CASSI or SSCSI). However an interesting problem would be to optimize the dictionary used in the sensing matrix. New methods exploiting the low rank properties of HS images (e.g., using the linear mixing model) would also deserved to be explored. Finally, determining the optimal number of measurements from the two images in order to optimize an appropriate fusion criterion is also an interesting prospect, which was suggested by one of the reviewers of this paper.

## REFERENCES

[1] J. M. Bioucas-Dias, A. Plaza, G. Camps-Valls, P. Scheunders, N. M. Nasrabadi, and J. Chanussot, “Hyperspectral remote sensing data analysis and future challenges,” *IEEE Geosci. Remote Sens. Mag.*, vol. 1, no. 2, pp. 6–36, Jun. 2013.

[2] Z. Xiong, A. Xie, D.-W. Sun, X.-A. Zeng, and D. Liu, “Applications of hyperspectral imaging in chicken meat safety and quality detection and evaluation: A review,” *Crit. Rev. Food Sci. Nutrition*, vol. 55, no. 9, pp. 1287–1301, Apr. 2014.

[3] J. P. Ryan, C. O. Davis, N. B. Tufillaro, R. M. Kudela, and B.-C. Gao, “Application of the hyperspectral imager for the coastal ocean to phytoplankton ecology studies in Monterey bay, CA, USA,” *Remote Sens.*, vol. 6, no. 2, pp. 1007–1025, Jan. 2014.

[4] G. J. Bellante, S. L. Powell, R. L. Lawrence, K. S. Repasky, and T. O. Dougher, “Aerial detection of a simulated $CO_2$ leak from a geologic sequestration site using hyperspectral imagery,” *Int. J. Greenhouse Gas Control*, vol. 13, pp. 124–137, Mar. 2013.

[5] G. Lu and B. Fei, “Medical hyperspectral imaging: A review,” *J. Biomed. Opt.*, vol. 19, no. 1, p. 10901, Jan. 2014.

[6] L. Loncan *et al.*, “Hyperspectral pansharpening: A review,” *IEEE Trans. Geosci. Remote Sens.*, vol. 3, no. 3, pp. 27–46, Sep. 2015.

[7] G. R. Arce, D. J. Brady, L. Carin, H. Arguello, and D. S. Kittle, “Compressive coded aperture spectral imaging: An introduction,” *IEEE Signal Process. Mag.*, vol. 31, no. 1, pp. 105–115, Jan. 2014.

[8] H. Arguello and G. R. Arce, “Colored coded aperture design by concentration of measure in compressive spectral imaging,” *IEEE Trans. Image Process.*, vol. 23, no. 4, pp. 1896–1908, Apr. 2014.

[9] E. J. Candès and M. B. Wakin, “An introduction to compressive sampling,” *IEEE Signal Process. Mag.*, vol. 25, no. 2, pp. 21–30, Mar. 2008.

[10] A. Wagadarikar, R. John, R. Willett, and D. Brady, “Single disperser design for coded aperture snapshot spectral imaging,” *Appl. Opt.*, vol. 47, no. 10, pp. B44–B51, Apr. 2008.

[11] X. Lin, Y. Liu, J. Wu, and Q. Dai, “Spatial-spectral encoded compressive hyperspectral imaging,” *ACM Trans. Graph.*, vol. 33, no. 6, pp. 233:1–233:11, Nov. 2014.

[12] G. Martín, J. M. Bioucas-Dias, and A. Plaza, “HYCA: A new technique for hyperspectral compressive sensing,” *IEEE Trans. Geosci. Remote Sens.*, vol. 53, no. 5, pp. 2819–2831, May 2015.

[13] J. E. Fowler, “Compressive-projection principal component analysis,” *IEEE Trans. Image Process.*, vol. 18, no. 10, pp. 2230–2242, Oct. 2009.

[14] Q. Wei, J. Bioucas-Dias, N. Dobigeon, and J. Y. Tourneret, "Hyperspectral and multispectral image fusion based on a sparse representation," *IEEE Trans. Geosci. Remote Sens.*, vol. 53, no. 7, pp. 3658–3668, Jul. 2015.

[15] D. Needell and R. Ward, "Stable image reconstruction using total variation minimization," *SIAM J. Imag. Sci.*, vol. 6, no. 2, pp. 1035–1058, Mar. 2013.

[16] Q. Wei, J. Bioucas-Dias, N. Dobigeon, and J.-Y. Tourneret, "Hyperspectral and multispectral image fusion based on a sparse representation," *IEEE Trans. Geosci. Remote Sens.*, vol. 53, no. 7, pp. 3658–3668, Jul. 2015.

[17] Q. Wei, N. Dobigeon, and J. Y. Tourneret, "Bayesian fusion of multiband images," *IEEE J. Sel. Topics Signal Process.*, vol. 9, no. 6, pp. 1117–1127, Sep. 2015.

[18] Q. Wei, S. Godsill, J. M. Bioucas-Dias, N. Dobigeon, and J.-Y. Tourneret, "High-resolution hyperspectral image fusion based on spectral unmixing," in *Proc. 19th Int. Conf. Inf. Fusion (FUSION)*, Heidelberg, Germany, Jul. 2016, pp. 1714–1719.

[19] N. Yokoya and A. Iwasaki, "Hyperspectral and multispectral data fusion mission on hyperspectral imager suite (HISUI)," in *Proc. IEEE Int. Symp. Geosci. Remote Sens. (IGARSS)*, Melbourne, VIC, Australia, Jul. 2013, pp. 4086–4089.

[20] X. Luo, J. Zhang, J. Yang, and Q. Dai, "Classification-based image-fusion framework for compressive imaging," *J. Electron. Imag.*, vol. 19, no. 3, p. 033009, Jul. 2010.

[21] H. Yin, Z. Liu, B. Fang, and Y. Li, "A novel image fusion approach based on compressive sensing," *Opt. Commun.*, vol. 354, pp. 299–313, Nov. 2015.

[22] I. August, Y. Oiknine, M. AbuLeil, I. Abdulhalim, and A. Stern, "Miniature compressive ultra-spectral imaging system utilizing a single liquid crystal phase retarder," *Sci. Rep.*, vol. 6, Mar. 2016, Art. no. 23524.

[23] H. Bai, G. Li, S. Li, Q. Li, Q. Jiang, and L. Chang, "Alternating optimization of sensing matrix and sparsifying dictionary for compressed sensing," *IEEE Trans. Signal Process.*, vol. 63, no. 6, pp. 1581–1594, Mar. 2015.

[24] A. P. Cuadros, C. Peitsch, H. Arguello, and G. R. Arce, "Coded aperture optimization for compressive X-ray tomosynthesis," *Opt. Express*, vol. 23, no. 25, pp. 32788–32802, Dec. 2015.

[25] C. V. Correa, H. Arguello, and G. R. Arce, "Spatiotemporal blue noise coded aperture design for multi-shot compressive spectral imaging," *J. Opt. Soc. Amer. A, Opt. Image Sci.*, vol. 33, no. 12, pp. 2312–2322, 2016.

[26] N. B. Bras, J. Bioucas-Dias, R. C. Martins, and A. C. Serra, "An alternating direction algorithm for total variation reconstruction of distributed parameters," *IEEE Trans. Image Process.*, vol. 21, no. 6, pp. 3004–3016, Jun. 2012.

[27] S. Boyd, N. Parikh, E. Chu, B. Peleato, and J. Eckstein, "Distributed optimization and statistical learning via the alternating direction method of multipliers," *Found. Trends Mach. Learn.*, vol. 3, no. 1, pp. 1–122, Jan. 2011.

[28] B. Kunkel, F. Blechinger, D. Viehmann, H. Van Der Piepen, and R. Doerffer, "ROSIS imaging spectrometer and its potential for ocean parameter measurements (airborne and space-borne)," *Int. J. Remote Sens.*, vol. 12, no. 4, pp. 753–761, Apr. 1991.

[29] Á. Barbero and S. Sra. (Nov. 2014). "Modular proximal optimization for multidimensional total-variation regularization." [Online]. Available: https://arxiv.org/abs/1411.0589

[30] Z. Wang and A. C. Bovik, "A universal image quality index," *IEEE Signal Process. Lett.*, vol. 9, no. 3, pp. 81–84, Mar. 2002.

[31] L. Wald, "Quality of high resolution synthesised images: Is there a simple criterion?" in *Proc. 3rd Conf. Fusion Earth Data, Merging Point Meas., Raster Maps Remotely Sensed Images (SEE/URISCA)*, 2000, pp. 99–103.

[32] T. Wan, N. Canagarajah, and A. Achim, "Compressive image fusion," in *Proc. 15th Int. Conf. Image Process. (ICIP)*, San Diego, CA, USA, Oct. 2008, pp. 1308–1311.

[33] R. Gao, S. A. Vorobyov, and H. Zhao, "Image fusion with cosparse analysis operator," *IEEE Signal Process Lett.*, vol. 24, no. 7, pp. 943–947, Jul. 2017.

[34] E. Vargas, Ó. Espitia, H. Arguello, and J.-Y. Tourneret, "Technical report associated with the paper 'Spectral image fusion from compressive measurements,"' Univ. Toulouse, Toulouse, France, Tech. Rep., Nov. 2018. [Online]. Available: http://tourneret.perso.enseeiht.fr/publis_fichiers/technical_report.pdf%

[35] R. O. Green *et al.*, "Imaging spectroscopy and the airborne visible/infrared imaging spectrometer (AVIRIS)," *Remote Sens. Environ.*, vol. 65, no. 3, pp. 227–248, Sep. 1998.

[36] M. Pereyra *et al.*, "A survey of stochastic simulation and optimization methods in signal processing," *IEEE J. Sel. Topics Signal Process.*, vol. 10, no. 2, pp. 224–241, Mar. 2016.

[37] J. Eckstein and D. F. Bertsekas, "On the Douglas–Rachford splitting method and the proximal point algorithm for maximal monotone operators," *Math. Program.*, vol. 55, nos. 1–3, pp. 293–318, 1992.

**Edwin Vargas** received the B.S. degree in electronic engineering from the Universidad Industrial de Santander, Bucaramanga, Colombia, in 2016, where he is currently pursuing the master's degree with the Department of the Electrical and Computer Engineering. His research interests focus on the areas of high dimensional signal processing, compressive sensing, and dictionary learning.

**Henry Arguello** (SM'17) received the master's degree in electrical engineering from the Universidad Industrial de Santander, Bucaramanga, Colombia, and the Ph.D. degree from the Electrical and Computer Engineering Department, University of Delaware, Newark. He is currently a Titular Professor with the Systems Engineering Department, Universidad Industrial de Santander. His current research interests include statistical signal processing, high dimensional signal coding and processing, optical imaging, optical code design, and computational imaging.

**Jean-Yves Tourneret** (SM'08) received the Ingénieur degree in electrical engineering from the École Nationale Supérieure d'Electronique, d'Electrotechnique, d'Informatique, d'Hydraulique et des Télécommunications (ENSEEIHT), Toulouse, in 1989, and the Ph.D. degree from the National Polytechnic Institute of Toulouse in 1992. He is currently a Professor with the University of Toulouse (ENSEEIHT) and a member of the IRIT Laboratory (UMR 5505 of the CNRS). His research activities are centered around statistical signal and image processing with a particular interest in Bayesian and Markov chain Monte Carlo methods. He has been a member of different technical committees, including the Signal Processing Theory and Methods Committee of the IEEE Signal Processing Society (2001–2007, 2010–2015) and the EURASIP SAT Committee on Theoretical and Methodological Trends in Signal Processing. He has been serving as an Associate Editor for IEEE TRANSACTIONS ON SIGNAL PROCESSING (2008–2011, 2015–present) and the *EURASIP Journal on Signal Processing* (2013–present).